

Suppression of Decoherence at Exceptional Transitions

Mei-Lin Li,^{*} Zuo Wang,^{*} and Liang He[†]

Institute for Theoretical Physics, School of Physics,

South China Normal University, Guangzhou 510006, China

*Key Laboratory of Atomic and Subatomic Structure and Quantum Control (Ministry of Education),
Guangdong Basic Research Center of Excellence for Structure and Fundamental Interactions of Matter,*

School of Physics, South China Normal University, Guangzhou 510006, China and

Guangdong Provincial Key Laboratory of Quantum Engineering and Quantum Materials,

Guangdong-Hong Kong Joint Laboratory of Quantum Matter,

South China Normal University, Guangzhou 510006, China

Decoherence is strongly influenced by environmental criticality, with conventional Hermitian critical points typically enhancing the loss of quantum coherence. Here, we show that this paradigm is fundamentally altered in non-Hermitian environments. Focusing on qubits coupled to non-Hermitian spin chains and interacting ultracold Fermi gases, we find that approaching exceptional points can either enhance or strongly suppress decoherence, depending on the balance between Hermitian and non-Hermitian system–environment couplings. In particular, when these couplings are comparable, decoherence is dramatically suppressed at exceptional transitions. We trace this behavior to the distinct response of the environmental ground state near non-Hermitian degeneracies and demonstrate the robustness of this effect across multiple models. Finally, we show that the predicted suppression of decoherence is directly observable on current digital quantum simulation platforms. Our results establish exceptional points as a concrete mechanism for suppressing decoherence and identify non-Hermitian criticality as a new avenue for coherence control in open quantum systems and quantum technologies.

Introduction.—The coherent superposition of quantum states—quantum coherence—marks one of the most fundamental distinctions between quantum mechanics and classical physics. It underlies entanglement, which plays an essential role in quantum computation and quantum information science [1]. Yet, in realistic settings, quantum systems may often lose coherence through interactions with their environments, a process known as decoherence [2, 3], thereby becoming effectively classical. Understanding decoherence is therefore of fundamental importance to the foundations of quantum physics [2, 3], as well as practical applications such as quantum engineering [1].

While environments are traditionally modeled as closed systems in this context [2–7], recent experimental advances have enabled the controlled engineering of tailored dissipative environments [8]. As it has been shown that dissipative environments can sometimes give rise to unconventional decoherence dynamics, including enhanced quantum coherence in the presence of strong dissipation [9]. This motivates us to revisit a prototypical problem of decoherence—namely, decoherence in the presence of environmental criticality [10]—in the new scenario.

Among dissipative environments, a case in point is non-Hermitian environments, i.e., those described by non-Hermitian Hamiltonians [11]. A hallmark feature of such environments is the existence of exceptional transitions [11, 12], which correspond to exceptional points

(EPs)—non-Hermitian degeneracies where two or more eigenvalues and eigenvectors coalesce [11]. Much like conventional quantum critical points, EPs can signal spectral gap closings and continuous phase transitions, as exemplified in the Lee–Yang model [13–15]. In conventional closed environments, decoherence is significantly enhanced near quantum critical points, as shown theoretically [16–22] and experimentally [23]. By contrast, dissipative environments can in some cases enhance coherence [9]. This contrast naturally raises the fundamental question of the fate of decoherence at exceptional transitions in non-Hermitian environments.

In this work, we address this question across diverse non-Hermitian environments, including spin chains and interacting ultracold Fermi gases, and find that decoherence induced by non-Hermitian environments exhibits behavior fundamentally distinct from that near Hermitian quantum critical points (see Fig. 1). More specifically, we find approaching EPs of non-Hermitian environments can either enhance [see Figs. 1(b2, c2), 2(b)] or strongly suppress decoherence [see Figs. 1(b1, c1), 2(a)], depending on the balance between Hermitian and non-Hermitian system–environment couplings. This behavior can be traced back to the distinct responses of the environmental ground state to different couplings. We further demonstrate the experimental observability of the decoherence suppression at exceptional transitions on current digital quantum computing platforms (see Fig. 3).

System and model.—We consider a central two-level system (qubit) coupled to a spin-chain environment, a setup widely used in decoherence studies [16–22] (see Fig. 1). In Hermitian environments, decoherence is strongly influenced by quantum criticality, where critical

^{*} These two authors contributed equally to this work.

[†] liang.he@sncnu.edu.cn

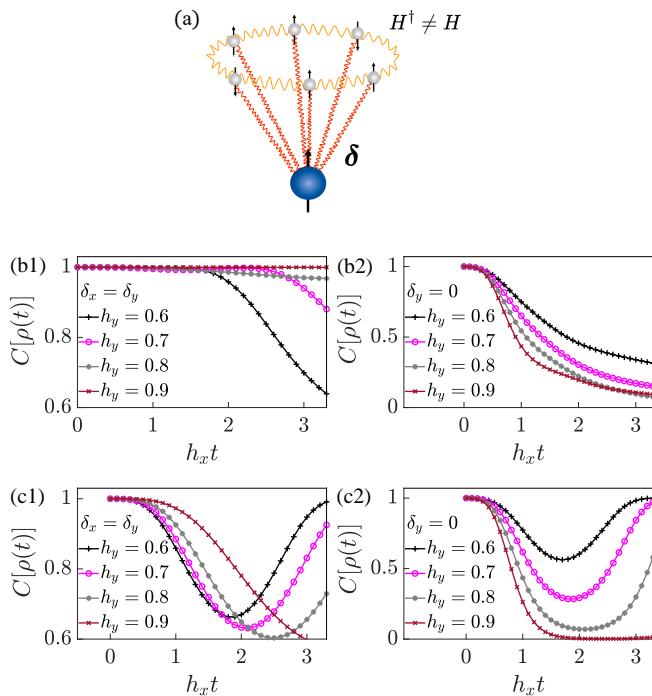


Figure 1. (a) Schematic illustration of a central qubit (system) coupled to its non-Hermitian environment formed by interacting spins in a complex transverse field. (b1, b2) Dynamics of qubit coherence $C[\rho(t)]$ as the non-Hermitian environment approaches its EPs, $h_y \rightarrow h_x = 1$. The environment is formed by an Ising chain with a complex transverse field [see Eq. (1)]. (b1) Coherence dynamics for balanced Hermitian and non-Hermitian system–environment couplings ($\delta_x = \delta_y$), showing pronounced suppression of decoherence near the EP. (b2) Coherence dynamics in the absence of non-Hermitian coupling ($\delta_y = 0$), showing the conventional enhancement of decoherence near the EP. (c1, c2) Same as (b1, b2), but for a non-Hermitian environment formed by Heisenberg spin chain in a complex transverse field. All simulations use $N = 25$, $J = 1/2$, $h_x = 1$, and $\sqrt{\delta_x^2 + \delta_y^2} = 0.1$. See text for more details.

fluctuations enhance the loss of coherence of the qubit [16–22]. Extensions to dissipative baths have further shown that dissipation can even protect coherence [9].

Here, we instead study a non-Hermitian environment described by a complex transverse-field Ising chain with periodic boundary conditions,

$$H_{\text{NI}} = - \sum_{j=1}^N [JZ_j Z_{j+1} + (h_x X_j + i h_y Y_j)], \quad (1)$$

where X , Y , and Z denote the Pauli operators, J is the interaction strength, and $\mathbf{h} \equiv (h_x, h_y)$ characterizes the strength of the complex transverse field in the (x, y) plane, with h_x and h_y real. The imaginary component of the transverse field can be effectively implemented via measurement and post-selection protocols [24]. The Hamiltonian H_{NI} assumes a real spectrum for $|h_y| < |h_x|$, but becomes non-diagonalizable at $h_y = \pm h_x$, corre-

sponding to EPs [24]. These EPs exhibit distinct non-Hermitian features, such as nontrivial topology and dimensional reduction [25–27], while also resembling Hermitian critical points through gap closing.

Decoherence generally arises from the coupling between the system and its environment. Since the environment considered here is non-Hermitian, we allow for both Hermitian and non-Hermitian system–environment couplings. The total Hamiltonian reads

$$H = H_{\text{NI}} - |1\rangle\langle 1| \otimes \sum_{j=1}^N (\delta_x X_j + i \delta_y Y_j), \quad (2)$$

where $|0\rangle$ and $|1\rangle$ denote the ground and excited states of the qubit, respectively. The parameters δ_x and δ_y are real and characterize the strengths of the Hermitian and non-Hermitian couplings.

In contrast to the conventional scenario—where both the environment and the system–environment coupling are Hermitian and enhanced decoherence is typically observed near the quantum critical point [16–22]—the interplay between Hermitian and non-Hermitian dynamics in our model leads to qualitatively different behavior. As we demonstrate below, near the exceptional transitions of the non-Hermitian environment, decoherence can instead be strongly suppressed.

Suppression of decoherence at EPs.—To analyze the decoherence of the qubit, we consider an initial state in which the qubit is prepared in the superposition $(|0\rangle + |1\rangle)/\sqrt{2}$, while the environment is in its ground state $|G\rangle_{\text{E}}$. We quantify the coherence of the qubit using the ℓ_1 -norm of coherence, defined as $C[\rho(t)] \equiv \sum_{i \neq j} |\rho_{ij}(t)|$ [28]. Here, $\rho(t)$ denotes the reduced density matrix of the qubit at time t , obtained by tracing out the environmental degrees of freedom, $\rho(t) = \text{tr}_{\text{E}} [|\psi(t)\rangle\langle\psi(t)| / \langle\psi(t)|\psi(t)\rangle]$, where $|\psi(t)\rangle$ is the state of the total system.

We first consider the case in which only Hermitian system–environment coupling is present, i.e., $\delta_y = 0$. As shown in Fig. 1(b2), when the non-Hermitian environment H_{NI} approaches its exceptional transition ($h_y \rightarrow h_x$), the coherence of the qubit decays more rapidly. This behavior resembles the enhanced decoherence observed near quantum critical points in conventional Hermitian environment [16–22].

In contrast, when both Hermitian and non-Hermitian system–environment couplings are present, the coherence dynamics change qualitatively. Fig. 1(b1) shows the time evolution of the coherence for equal coupling strengths, $\delta_x = \delta_y$. As the environment approaches its exceptional transition ($h_y \rightarrow h_x$), decoherence is not enhanced but instead strongly suppressed. This result highlights a key distinction from Hermitian environments, where decoherence is typically amplified near critical points. In non-Hermitian environments, exceptional transitions can instead lead to coherence protection.

To examine whether this suppression is specific to the above non-Hermitian Ising environment, we next

consider another non-Hermitian environment which is formed by a non-Hermitian spin-1/2 Heisenberg chain described by

$$H_{\text{NH}} = H_{\text{XXX}} - \sum_{j=1}^N (h_x X_j + i h_y Y_j), \quad (3)$$

where $H_{\text{XXX}} \equiv -J \sum_{j=1}^N (X_j X_{j+1} + Y_j Y_{j+1} + Z_j Z_{j+1})$ is the isotropic Heisenberg Hamiltonian with periodic boundary conditions. As in the Ising case, H_{NH} assumes a completely real spectrum for $|h_y| < |h_x|$ and exhibits EPs at $h_y = \pm h_x$ [24]. We consider the same form of system–environment coupling as in the non-Hermitian Ising case [see the second term in Eq. (2)]. The coherence dynamics for $\delta_x = \delta_y$ are shown in Fig. 1(c1). Similar to the Ising case, decoherence is strongly suppressed as the environment approaches its exceptional transition. This suggests that decoherence suppression near exceptional points is a generic feature of non-Hermitian environments.

To understand the underlying mechanism, we note that in the absence of the transverse field, the ferromagnetic Ising and Heisenberg chains both possess a doubly degenerate ground-state manifold consisting of fully polarized states. The complex transverse field term, $-\sum_{j=1}^N (h_x X_j + i h_y Y_j)$, lifts this degeneracy. In particular, at the EPs (e.g., $h_x = h_y$), a unique polarized ground state $|G\rangle_{\text{E}}$ is selected. In general, system–environment coupling can drive the environment away from this polarized ground state, inducing strong environmental fluctuations and thereby enhancing decoherence near the exceptional transition. However, when the Hermitian and the non-Hermitian system–environment couplings assume the same strength, we find that the coupling cannot drive the environment away from $|G\rangle_{\text{E}}$ (see Supplementary Material [29] for details). As a result, environmental fluctuations are suppressed, leading to reduced decoherence. Away from the EPs, an analytic treatment becomes intractable; nevertheless, extensive numerical simulations confirm that decoherence suppression remains robust in their vicinity (see Supplementary Material [29]).

Suppression of decoherence at EPs of a non-Hermitian ultracold-gas environment.—The preceding section demonstrated that decoherence suppression at EPs is a generic feature of non-Hermitian environments, although the discussion was restricted to spin systems. We now turn to a qualitatively different class of non-Hermitian environments formed by ultracold gases in optical lattices, which are closely connected to experimental realizations of non-Hermitian quantum systems [30–33]. Specifically, we consider a non-Hermitian environment consisting of ultracold Fermi gases in a one-dimensional

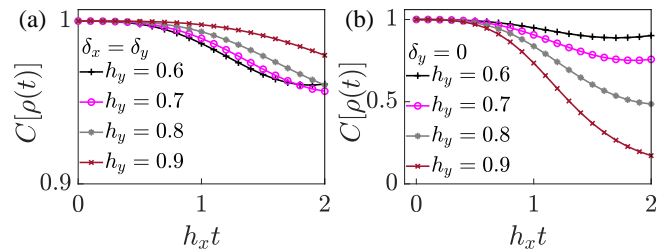


Figure 2. Dynamics of qubit coherence $C[\rho(t)]$ as a non-Hermitian environment formed by Fermi gases in optical lattices approaches its EPs, $h_y \rightarrow h_x = 1$. (a) Coherence dynamics for balanced Hermitian and non-Hermitian system–environment couplings ($\delta_x = \delta_y$), showing pronounced suppression of decoherence near the EP. (b) Coherence dynamics in the absence of non-Hermitian coupling ($\delta_y = 0$), showing the conventional enhancement of decoherence near the EP. All simulations use $N = 10$, $J = 0.1$, $U = 0.4$, $h_x = 1$, $\sqrt{\delta_x^2 + \delta_y^2} = 0.1$. See text for more details.

optical lattice, described by the Hamiltonian

$$H_{\text{NF}} = -J \sum_j^N \sum_{\sigma=\uparrow,\downarrow} (c_{j,\sigma}^\dagger c_{j+1,\sigma} + \text{h.c.}) + U \sum_{j=1}^N n_{j,\uparrow} n_{j,\downarrow} + h_x \sum_{j=1}^N (c_{j,\downarrow}^\dagger c_{j,\uparrow} + \text{h.c.}) - i h_y \sum_{j=1}^N (n_{j,\uparrow} - n_{j,\downarrow}), \quad (4)$$

where $c_{j,\sigma}^\dagger$ creates a fermion with spin $\sigma \in \{\uparrow, \downarrow\}$ at site j , and $n_{j,\sigma} \equiv c_{j,\sigma}^\dagger c_{j,\sigma}$. The first two terms describe nearest-neighbor hopping with amplitude J and on-site interaction with strength U , respectively. The third term represents spin-flip (Rabi) processes, while the last term introduces spin-dependent gain and loss, rendering the Hamiltonian non-Hermitian. The spectrum of H_{NF} is real for $|h_y| < |h_x|$, and an EP occurs at $h_y = h_x$, where the Hamiltonian H_{NF} becomes non-diagonalizable [24].

We investigate the coherence dynamics of a qubit coupled to this non-Hermitian Fermi gas through the total Hamiltonian $H_{\text{tot}} = H_{\text{NF}} + |1\rangle\langle 1| \otimes \sum_{j=1}^N [\delta_x (c_{j,\downarrow}^\dagger c_{j,\uparrow} + \text{h.c.}) - i \delta_y (n_{j,\uparrow} - n_{j,\downarrow})]$. This form models a situation where the environment evolves under H_{NF} when the qubit is in the ground state $|0\rangle$, but experiences modified Rabi driving and gain–loss processes when the qubit is in the excited state $|1\rangle$.

The resulting coherence dynamics are shown in Fig. 2. We observe behavior qualitatively similar to that found in the non-Hermitian spin-chain environments. In particular, when $\delta_x = \delta_y$, decoherence is strongly suppressed at the exceptional transition of the non-Hermitian Fermi gas environment [Fig. 2(a)]. These results identify ultracold Fermi gases as a promising experimental platform for observing decoherence suppression at EPs.

Observability on digital quantum computers.—In view of the rapid progress in digital quantum computing, the predicted coherence behavior should be experimentally

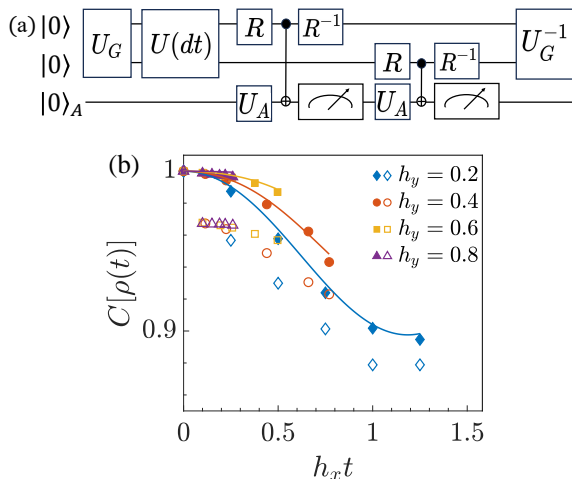


Figure 3. Simulation of qubit coherence dynamics on a quantum circuit, with the non-Hermitian environment formed by an Ising chain in a complex transverse field. (a) Quantum circuit protocol for simulating the first time step of the dynamics. (b) Coherence dynamics obtained from the quantum circuit. Hollow (solid) markers denote results from 2×10^6 trajectories on the *qasm_simulator* with (without) noise from *ibm_brisbane*, provided by IBM Qiskit [34]. Solid curves show exact results from numerical calculations. Simulations use $J = 1/100$, $h_x = 1$, $\delta_x = \delta_y = 0.5$, and an optimized time step dt . See text for more details.

accessible using current quantum simulators. As a concrete demonstration, we simulate the coherence dynamics of a system qubit coupled to a two-site non-Hermitian Ising chain serving as its environment, implemented as a quantum circuit in IBM Qiskit [34]. For the initial qubit state $(|0\rangle + |1\rangle)/\sqrt{2}$, the coherence $C[\rho(t)]$ is equivalent to the overlap between two time-evolved states of the environment (see [29]). This relation allows us to reduce the required quantum resources by simulating only the environmental dynamics.

The quantum circuit implementing the time evolution of the two-site non-Hermitian Ising chain is shown in Fig. 3(a). The environmental ground state $|G\rangle_E$ is prepared by applying a two-qubit unitary operator U_G to the initial state $|0\rangle \otimes |0\rangle$. The operator U_G can be implemented by three elementary single-qubit gates combined with a controlled-Z gate [29].

For a short time step dt , the time-evolution operator is Trotter decomposed into a unitary part $U(dt) \equiv e^{idtJ \sum_{j=1}^N Z_j Z_{j+1}} e^{idt(h_x + \delta_x) \sum_{j=1}^N X_j}$ and a non-unitary part $e^{-dt(h_y + \delta_y) \sum_{j=1}^N Y_j}$. The unitary part $U(dt)$ can be realized by standard one- and two-qubit gates. The nonunitary part is realized using a measurement-based protocol [35, 36] that employs an ancilla qubit [bottom row of Fig. 3(a)] together with projective measurement and postselection. Specifically, a single qubit unitary op-

erator $R \equiv (e^{i\pi/4}I + e^{-i\pi/4} \sum_{a=X,Y,Z} a)/2$ is applied to each qubit, followed by a CNOT gate and the inverse operation R^{-1} . The ancilla qubit is initialized via the rotation $U_A \equiv e^{-i(\pi/4 + (h_y + \delta_y)dt)Y}$. After the CNOT interaction, the ancilla is measured in the computational (Z) basis and the outcome $|0\rangle$ is postselected, as illustrated in Fig. 3(a). Finally, the overlap between two time-evolved environmental states is obtained by applying U_G^{-1} and collecting the final measurement statistics (see [29] for more details).

Fig. 3(b) demonstrates quantum circuit simulations of the coherence dynamics on IBM Qiskit [34] (discrete markers) and coherence dynamics by direct numerical simulations (solid curves). When the Hermitian and non-Hermitian system-environment couplings assume the same strength, the simulated coherence dynamics clearly exhibit decoherence suppression as the non-Hermitian environment approaches its exceptional transition, in agreement with our theoretical predictions.

Conclusion.—We have shown that decoherence induced by non-Hermitian environments exhibits behavior fundamentally distinct from that near Hermitian quantum critical points. Whereas Hermitian criticality typically enhances decoherence, approaching EPs of non-Hermitian environments can either enhance or strongly suppress decoherence, depending on the balance between Hermitian and non-Hermitian system-environment couplings. This establishes non-Hermitian criticality as a qualitatively new regime for decoherence dynamics. We demonstrated the generality of this effect across diverse non-Hermitian environments, including spin chains and interacting ultracold Fermi gases, and showed that the predicted behavior is directly accessible on current quantum simulation platforms. Our findings uncover an unexplored role of EPs in open quantum dynamics and identify non-Hermitian environments as a new avenue for controlling decoherence. More broadly, they suggest that engineered non-Hermitian criticality may serve as a practical resource for coherence protection in quantum information processing, sensing, and quantum simulation.

ACKNOWLEDGMENTS

We acknowledge the use of IBM Quantum services for this work. The views expressed are those of the authors, and do not reflect the official policy or position of IBM or the IBM Quantum team. This work is supported by the NKRDP (Grant No. 2022YFA1405304), NSFC (Grant No. 12275089), Guangdong Basic and Applied Basic Research Foundation (Grants No. 2023A1515012800), Guangdong Provincial Quantum Science Strategic Initiative (Grant No. GDZX2204003), and Guangdong Provincial Key Laboratory (Grant No. 2020B1212060066).

-
- [1] M. A. Nielsen and I. L. Chuang, *Quantum Computation and Quantum Information: 10th Anniversary Edition* (Cambridge University Press, 2010).
- [2] W. H. Zurek, Decoherence, einselection, and the quantum origins of the classical, *Rev. Mod. Phys.* **75**, 715 (2003).
- [3] M. Schlosshauer, Decoherence, the measurement problem, and interpretations of quantum mechanics, *Rev. Mod. Phys.* **76**, 1267 (2005).
- [4] A. O. Caldeira and A. J. Leggett, Influence of dissipation on quantum tunneling in macroscopic systems, *Phys. Rev. Lett.* **46**, 211 (1981).
- [5] A. J. Leggett, S. Chakravarty, A. T. Dorsey, M. P. A. Fisher, A. Garg, and W. Zwerger, Dynamics of the dissipative two-state system, *Rev. Mod. Phys.* **59**, 1 (1987).
- [6] H.-P. Breuer and F. Petruccione, *The Theory of Open Quantum Systems* (Oxford University Press, 2007).
- [7] H.-P. Breuer, E.-M. Laine, J. Piilo, and B. Vacchini, Colloquium: Non-markovian dynamics in open quantum systems, *Rev. Mod. Phys.* **88**, 021002 (2016).
- [8] P. M. Harrington, E. J. Mueller, and K. W. Murch, Engineered dissipation for quantum information science, *Nature Reviews Physics* **4**, 660 (2022).
- [9] M. Onizhuk, Y.-X. Wang, J. Nagura, A. A. Clerk, and G. Galli, Understanding central spin decoherence due to interacting dissipative spin baths, *Phys. Rev. Lett.* **132**, 250401 (2024).
- [10] D. Rossini and E. Vicari, Coherent and dissipative dynamics at quantum phase transitions, *Phys. Rep.* **936**, 1 (2021), coherent and dissipative dynamics at quantum phase transitions.
- [11] Z. G. Yuto Ashida and M. Ueda, Non-Hermitian physics, *Adv. Phys.* **69**, 249 (2020).
- [12] M. Fruchart, R. Hanai, P. B. Littlewood, and V. Vitelli, Non-reciprocal phase transitions, *Nature* **592**, 363 (2021).
- [13] G. von Gehlen, Critical and off-critical conformal analysis of the ising quantum chain in an imaginary field, *J. Phys. A: Math. Gen.* **24**, 5371 (1991).
- [14] O. A. Castro-Alvaredo and A. Fring, A spin chain model with non-hermitian interaction: the ising quantum spin chain in an imaginary field, *J. Phys. A: Math. Theor.* **42**, 465211 (2009).
- [15] K. Uzelac, P. Pfeuty, and R. Jullien, Yang-lee edge singularity from a real-space renormalization-group method, *Phys. Rev. Lett.* **43**, 805 (1979).
- [16] H. T. Quan, Z. Song, X. F. Liu, P. Zanardi, and C. P. Sun, Decay of loschmidt echo enhanced by quantum criticality, *Phys. Rev. Lett.* **96**, 140604 (2006).
- [17] D. Rossini, T. Calarco, V. Giovannetti, S. Montangero, and R. Fazio, Decoherence induced by interacting quantum spin baths, *Phys. Rev. A* **75**, 032333 (2007).
- [18] Z.-G. Yuan, P. Zhang, and S.-S. Li, Disentanglement of two qubits coupled to an xy spin chain: Role of quantum phase transition, *Phys. Rev. A* **76**, 042118 (2007).
- [19] Z.-G. Yuan, P. Zhang, and S.-S. Li, Loschmidt echo and berry phase of a quantum system coupled to an xy spin chain: Proximity to a quantum phase transition, *Phys. Rev. A* **75**, 012102 (2007).
- [20] B. Damski, H. T. Quan, and W. H. Zurek, Critical dynamics of decoherence, *Phys. Rev. A* **83**, 062104 (2011).
- [21] E. Vicari, Decoherence dynamics of qubits coupled to systems at quantum transitions, *Phys. Rev. A* **98**, 052127 (2018).
- [22] D. Rossini and E. Vicari, Scaling of decoherence and energy flow in interacting quantum spin systems, *Phys. Rev. A* **99**, 052113 (2019).
- [23] J. Zhang, X. Peng, N. Rajendran, and D. Suter, Detection of quantum critical points by a probe qubit, *Phys. Rev. Lett.* **100**, 100501 (2008).
- [24] Z. Wang, S.-L. Zhu, L.-J. Lang, and L. He, Measurement-induced integer families of critical dynamical scaling in quantum many-body systems, [arXiv:2308.06567](https://arxiv.org/abs/2308.06567).
- [25] E. J. Bergholtz, J. C. Budich, and F. K. Kunst, Exceptional topology of non-hermitian systems, *Rev. Mod. Phys.* **93**, 015005 (2021).
- [26] K. Ding, C. Fang, and G. Ma, Non-hermitian topology and exceptional-point geometries, *Nat. Rev. Phys.* **4**, 745 (2022).
- [27] H. Hu, S. Sun, and S. Chen, Knot topology of exceptional point and non-hermitian no-go theorem, *Phys. Rev. Res.* **4**, L022064 (2022).
- [28] T. Baumgratz, M. Cramer, and M. B. Plenio, Quantifying coherence, *Phys. Rev. Lett.* **113**, 140401 (2014).
- [29] See Supplemental Material for a discussion on relevant technical details.
- [30] R. Jördens, N. Strohmaier, K. Günter, H. Moritz, and T. Esslinger, A mott insulator of fermionic atoms in an optical lattice, *Nature* **455**, 204 (2008).
- [31] A. Mazurenko, C. S. Chiu, G. Ji, M. F. Parsons, M. Kanász-Nagy, R. Schmidt, F. Grusdt, E. Demler, D. Greif, and M. Greiner, A cold-atom fermi-hubbard antiferromagnet, *Nature* **545**, 462 (2017).
- [32] M. Boll, T. A. Hilker, G. Salomon, A. Omran, J. Nespolo, L. Pollet, I. Bloch, and C. Gross, Spin- and density-resolved microscopy of antiferromagnetic correlations in fermi-hubbard chains, *Science* **353**, 1257 (2016).
- [33] M. Schreiber, S. S. Hodgman, P. Bordia, H. P. Lüschen, M. H. Fischer, R. Vosk, E. Altman, U. Schneider, and I. Bloch, Observation of many-body localization of interacting fermions in a quasirandom optical lattice, *Science* **349**, 842 (2015).
- [34] A. Cross, The ibm q experience and qiskit open-source quantum computing software, in *APS March meeting abstracts*, Vol. 2018 (2018) pp. L58–003.
- [35] T. A. Brun, L. Diósi, and W. T. Strunz, Test of weak measurement on a two- or three-qubit computer, *Phys. Rev. A* **77**, 032101 (2008).
- [36] Z. Wang and L. He, Emergent non-hermitian conservation laws at exceptional points, *Phys. Rev. B* **111**, L100305 (2025).
- [37] H. Zhao, M. Bukov, M. Heyl, and R. Moessner, Making trotterization adaptive and energy-self-correcting for nisq devices and beyond, *PRX Quantum* **4**, 030319 (2023).
- [38] H. Zhao, M. Bukov, M. Heyl, and R. Moessner, Adaptive trotterization for time-dependent hamiltonian quantum dynamics using piecewise conservation laws, *Phys. Rev. Lett.* **133**, 010603 (2024).

Supplemental Material for ‘‘Suppression of Decoherence at Exceptional Transitions’’

The supplemental material provides additional numerical and analytical results supporting the main text. We present the coherence dynamics of the qubit for relevant non-Hermitian system–environment couplings and show that suppression of decoherence near the exceptional transition is robust over a finite parameter region. We further analyze the overlap of time-evolved environmental states and demonstrate that the non-Hermitian dynamics dynamically selects a unique polarized environmental ground state, thereby suppressing decoherence. Finally, we provide implementation details for the digital quantum simulation in IBM Qiskit, including state preparation, ancilla-assisted postselection for nonunitary evolution, time-step optimization, and data-processing procedures.

S1. DECOHERENCE DYNAMICS FOR DIFFERENT COUPLINGS

In this section, we show that suppression of decoherence near the exceptional transition at $\delta_x = \delta_y$ is robust over a finite parameter region. We parameterize the non-Hermitian system–environment couplings δ by an angle θ via $(\delta_x, \delta_y) = |\delta|(\sin \theta, \cos \theta)$ and present the numerical simulation results that reveal the detailed behavior of $C[\rho(t)]$ decay near EP, located around $\theta = \pi/4$ in the real energy spectrum. Fig. S1 presents the dynamics of $C[\rho(t)]$ near EP, with particular attention to the transitional regions between enhanced and suppressed decay, which emerge as the angle is tuned across $\pi/4$. To isolate the role of the complex field component h_y , we fix its value at $h_y = 0.9$, allowing us to focus on $C[\rho(t)]$ behavior within the range $\theta \in [0, \pi/2)$. As shown in Fig. S2, the $C[\rho(t)]$ decay exhibits a symmetric distribution around $\theta = \pi/4$ near EP. Deviations from either side of this angle lead to more enhanced decay, indicating that $\theta = \pi/4$ corresponds to a special, decay-minimizing coupling scenario. To demonstrate the robustness of this suppressed decay of $C[\rho(t)]$, we also consider couplings with parameter θ close to $\pi/4$, as shown in Fig. S2. These results confirm that the contrasting behavior exactly at $\theta = \pi/4$ is not a fine-tuned artifact, but a physically robust phenomenon observable in a finite parameter region.

S2. GROUND-STATE SUSCEPTIBILITY NEAR THE EPS

In this section, we demonstrate how the non-Hermitian dynamics dynamically selects a unique polarized environmental ground state. To quantify the ground-state sensitivity, we define the ground-state *susceptibility* via the

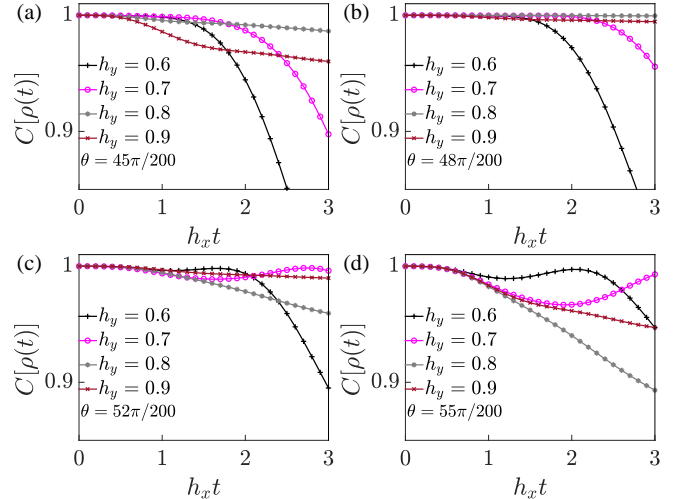


Figure S1. Dynamics of the qubit coherence $C[\rho(t)]$ as a non-Hermitian environment formed by a non-Hermitian Ising model under different coupling strengths $\delta_x = |\delta| \sin \theta$ and $\delta_y = |\delta| \cos \theta$ approaches its EPs, $h_y \rightarrow h_x = 1$. (a-d) The $C[\rho(t)]$ for time $t \in [0, 3]$ with $\theta = 45\pi/200$ (a), $\theta = 48\pi/200$ (b), $\theta = 52\pi/200$ (c), $\theta = 55\pi/200$ (d). All simulations use $N = 25$ and $J = 1/2$, $h_x = 1$, $|\delta| = \sqrt{\delta_x^2 + \delta_y^2} = 0.1$. See text for more details.

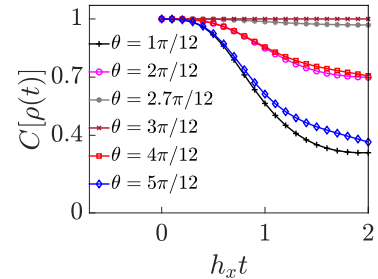


Figure S2. Dynamics of the qubit coherence $C[\rho(t)]$ as a non-Hermitian environment formed by a non-Hermitian Ising model with fixed complex field h_y under different θ . All simulations use $N = 25$ and $h_y = 0.9$, $J = 1/2$, $h_x = 1$ under different couplings $\delta_x = |\delta| \sin \theta$, $\delta_y = |\delta| \cos \theta$, $|\delta| = \sqrt{\delta_x^2 + \delta_y^2} = 0.1$. See text for more details.

overlap between the perturbed and unperturbed ground states:

$$\chi(\mathbf{h}, \delta) = -\ln |\langle G(\mathbf{h} + \delta) | G(\mathbf{h}) \rangle|. \quad (\text{S1})$$

where $\mathbf{h} \equiv (h_x, h_y)$ characterizes the strength of the complex transverse field in the (x, y) plane, with both h_x and h_y being real numbers. We numerically evaluate this susceptibility over a range of (h_x, h_y) values for two coupling types: (i) $\delta_x = \delta_y$ and (ii) $\delta_y = 0$, using the same parameters as in Fig. 1. As shown in Figs. S3(a, c), when

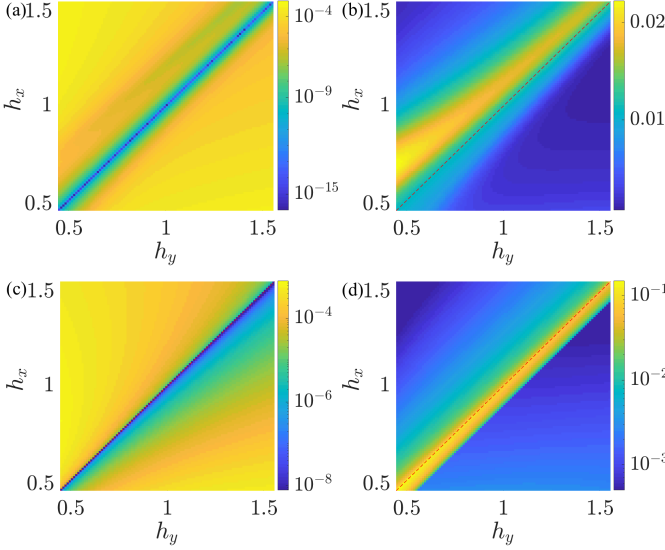


Figure S3. Ground-state susceptibility near EP for the non-Hermitian Ising and Heisenberg model under a complex transverse field. (a–b) Susceptibility $\chi(\mathbf{h}, \boldsymbol{\delta})$ for the non-Hermitian Ising model with $\delta_x = \delta_y$ (a) and $\delta_y = 0$ (b) for $N = 8$. (c–d) Susceptibility for the non-Hermitian Heisenberg model with $\delta_x = \delta_y$ (c) and $\delta_y = 0$ (d) for $N = 4$. All simulations use $J = 1/2$ and $|\boldsymbol{\delta}| = \sqrt{\delta_x^2 + \delta_y^2} = 0.1$.

$\delta_x = \delta_y$, the susceptibility χ is minimized near the exceptional line (the locus of EPs in parameter space), indicating that the ground state is particularly robust against such perturbations. This observation explains the suppressed $C[\rho(t)]$ decay in Figs. 1(b1, c1). In contrast, for $\delta_y = 0$, Figs. S3(b, d) show that χ increases as the system approaches the exceptional line from the $h_x > h_y$ side. On the $h_x < h_y$ side, the susceptibility decreases for the Heisenberg model but increases for the Ising model.

S3. QUANTUM CIRCUIT PROTOCOL

In this section, we show how the coherence $C[\rho(t)]$ can be directly measured within a quantum circuit. With the initial qubit state $(|0\rangle + |1\rangle)/\sqrt{2}$, the total system–environment state is expressed as $|\psi(t)\rangle = \frac{1}{\sqrt{2}}(|0\rangle \otimes |\varphi_0(t)\rangle + |1\rangle \otimes |\varphi_\delta(t)\rangle)$. Substituting the qubit’s reduced density matrix $\rho(t)$ (obtained by tracing out the environmental degrees of freedom) into the ℓ_1 norm of the coherence $C[\rho(t)] \equiv \sum_{i \neq j} |\rho_{ij}(t)|$ yields $C[\rho(t)] = |\langle \varphi_0(t) | \varphi_\delta(t) \rangle| / |\langle \psi(t) | \psi(t) \rangle|$, showing that the ℓ_1 norm of the qubit’s coherence is equivalent to the overlap between the two time-evolved environmental states.

A. Preparation of the initial state

In this subsection, we detail the implementation of the operations U_G and U_G^{-1} shown in Fig. 3(a). Specifically,

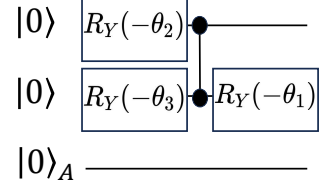


Figure S4. Quantum circuit realization of U_G in Fig. 3(a).

we begin by constructing the inverse operation U_G^{-1} , which maps the ground state $|G\rangle_E$ to the initial product state $|0\rangle \otimes |0\rangle$. The unitary operation U_G , which prepares the ground state, can then be obtained by reversing this procedure. The inverse operation U_G^{-1} consists of three single-qubit rotation gates $R_Y(\theta_1), R_Y(\theta_2), R_Y(\theta_3)$, along with a CZ gate. To begin, the process starts from the ground state $|G\rangle_E \equiv \xi_0|00\rangle + \xi_1|01\rangle + \xi_2|10\rangle + \xi_3|11\rangle$.

First, the circuit begins by applying a rotation gate $R_Y(\theta_1)$ to the second qubit, followed by a CZ gate applying on both qubits. This sequence transforms the initial state $|G\rangle_E$ into the intermediate state:

$$|\varphi_1\rangle = U_{CZ} (I \otimes R_Y(\theta_1)) |G\rangle_E, \quad (\text{S2})$$

where the rotation angle is defined as $\theta_1 = 2 \arctan((\xi_2 - k\xi_0) / (\xi_3 - k\xi_1))$ and $k = -\text{sign}(\xi_0\xi_2 + \xi_1\xi_3) \sqrt{(\xi_2^2 + \xi_3^2) / (\xi_0^2 + \xi_1^2)}$, with $\text{sign}(x) \equiv x/|x|$ for $x \neq 0$.

The resulting state can be written as a tensor product:

$$|\varphi_1\rangle \equiv (a_0|0\rangle + a_1|1\rangle) \otimes (a_2|0\rangle + a_3|1\rangle),$$

where the parameters are defined in terms of the original ground state amplitudes ξ_i :

$$a_0 = 1/\sqrt{1+k^2}, \quad (\text{S3})$$

$$a_1 = k/\sqrt{1+k^2}, \quad (\text{S4})$$

$$a_2 = \sqrt{1+k^2} (-\xi_1\xi_2 + \xi_0\xi_3) / \varsigma, \quad (\text{S5})$$

$$a_3 = \sqrt{1+k^2} [k(\xi_0\xi_2 + \xi_1\xi_3) - (\xi_2^2 + \xi_3^2)] / k\varsigma, \quad (\text{S6})$$

with the normalization factor $\varsigma \equiv \sqrt{(-k\xi_0 + \xi_2)^2 + (-k\xi_1 + \xi_3)^2}$. This transformation disentangles the ground state, yielding a fully separable product form.

Second, the rotation gate $R_Y(\theta_2)$ is applied to the first qubit,

$$|\varphi_2\rangle = (R_Y(\theta_2) \otimes I) |\varphi_1\rangle \equiv \gamma_0|00\rangle + \gamma_1|01\rangle, \quad (\text{S7})$$

where the amplitudes are given by

$$\gamma_0 = \frac{(a_0a_3 + ka_1a_3)(-\xi_1\xi_2 + \xi_0\xi_3)}{\tau}, \quad (\text{S8})$$

$$\gamma_1 = \frac{a_1a_3(k\xi_0\xi_2 - \xi_2^2 + k\xi_1\xi_3 - \xi_3^2)}{\tau} + \frac{a_0a_3(-k\xi_0^2 + \xi_0\xi_2 - k\xi_1^2 + \xi_1\xi_3)}{\tau}, \quad (\text{S9})$$

and the normalization factor is

$$\tau \equiv \sqrt{\left((a_0 a_3)^2 + (a_1 a_3)^2\right) \left[(-k\xi_0 + \xi_2)^2 + (-k\xi_1 + \xi_3)^2\right]}. \quad (\text{S10})$$

The rotation angle is defined as $\theta_2 = 2 \arctan(-a_1 a_3 / a_0 a_3)$. This step rotates the first qubit from the X -basis to the Z -basis, mapping $|+\rangle = (|0\rangle + |1\rangle) / \sqrt{2}$ onto $|0\rangle$. The two-qubit state is projected into the subspace spanned by $|00\rangle$ and $|01\rangle$, bringing it closer to the target product state $|0\rangle \otimes |0\rangle$.

Finally, a rotation gate $R_Y(\theta_3)$ is applied to the second qubit, yielding the final state

$$|00\rangle = (I \otimes R_Y(\theta_3)) |\varphi_2\rangle, \quad (\text{S11})$$

where the rotation angle is given by $\theta_3 = 2 \arctan(-\gamma_1 / \gamma_0)$. This final step completes the transformation from the ground state $|G\rangle_E$ to the fully separable state $|0\rangle \otimes |0\rangle$.

The corresponding ground-state preparation can be achieved by reversing the above procedure: the inverse sequence consists of applying the gates in reverse order, with each rotation angle negated. Specifically, the sequence begins with $R_Y(-\theta_2)$ on the first qubit and $R_Y(-\theta_3)$ on the second qubit. Subsequently, a CZ gate is applied, and finally $R_Y(-\theta_1)$ acts on the second qubit. This gate sequence realizes the unitary transformation that prepares the ground state $|G\rangle_E$, as illustrated in Fig. S4. In the main text, the ground state of the two-site non-Hermitian environment, is represented in the quantum circuit by the normalized column vector in the Z basis $[(h_x + h_y) / \beta, -\alpha / 2\beta, -\alpha / 2\beta, (h_x - h_y) / \beta]^T$, where $\alpha \equiv J - \sqrt{4h_x^2 - 4h_y^2 + J^2}$ and $\beta \equiv \sqrt{4h_x^2 + J\alpha}$.

B. Simulating the non-unitary dynamics

This subsection demonstrates how the quantum circuit shown in Fig. 3(a) simulates the non-unitary part of the dynamics in the two-site non-Hermitian Ising Hamiltonian (Eq. (1)), along with the associated data post-selection procedure [36]. In the first time interval dt , the unitary operation U_G prepares the ground state $|G\rangle_E$ from the initial product state $|0\rangle \otimes |0\rangle$. This is followed by unitary evolution under the operator $U(dt)$, resulting in an intermediate state expressed in the eigenbasis of Y . To fully implement the non-unitary evolution, an ancilla qubit is introduced. In the limit of small dt , the non-unitary part can be decomposed as

$$\begin{aligned} & \exp\left(-\tilde{d}t \sum_{j=1}^N Y_j\right) \\ & \approx \left(\frac{\cos \tilde{d}t}{\sqrt{2}}\right)^{-N} \prod_{j=1}^N \left(\frac{\cos \tilde{d}t}{\sqrt{2}} - \frac{\sin \tilde{d}t}{\sqrt{2}} P_{j,\uparrow_y} + \frac{\sin \tilde{d}t}{\sqrt{2}} P_{j,\downarrow_y}\right), \end{aligned} \quad (\text{S12})$$

where $\tilde{d}t = (h_y + \delta_y) dt$, $P_{j,\uparrow_y} \equiv (1 + Y_j) / 2$, $P_{j,\downarrow_y} \equiv (1 - Y_j) / 2$. Each non-unitary term $\left[\left(\cos \tilde{d}t / \sqrt{2}\right) - \left(\sin \tilde{d}t / \sqrt{2}\right) P_{j,\uparrow_y} + \left(\sin \tilde{d}t / \sqrt{2}\right) P_{j,\downarrow_y}\right]$ in the product is implemented via a sequence of quantum operations involving an ancilla qubit, which enables the effective non-unitary evolution through post-selection. The simulation proceeds as follows:

First, the ancilla qubit is initialized to the state

$$\begin{aligned} & e^{-i(\pi/4 + \tilde{d}t)Y} |0\rangle_A \\ & = \frac{1}{\sqrt{2}} \left(\cos \tilde{d}t - \sin \tilde{d}t\right) |0\rangle_A + \frac{1}{\sqrt{2}} \left(\cos \tilde{d}t + \sin \tilde{d}t\right) |1\rangle_A. \end{aligned} \quad (\text{S13})$$

Second, unitary rotations $R \equiv (e^{i\pi/4} I + e^{-i\pi/4} \sum_{a=X,Y,Z} a) / 2$ are applied to the first system qubit, such that $R|\uparrow_y\rangle(|\downarrow_y\rangle) = |\uparrow\rangle(|\downarrow\rangle)$, resulting in state $\sum_{Y_1, Z_2} c_{Y_1, Z_2} (R|Y_1\rangle) \otimes |Z_2\rangle$. Third, a controlled-NOT gate is applied between the first system qubit (control) and the ancilla qubit (target), resulting in the state:

$$\begin{aligned} & \sum_{Z_2} c_{\uparrow_y, Z_2} (R|\uparrow_y\rangle) \otimes |Z_2\rangle \otimes \left(e^{-i(\pi/4 + \tilde{d}t)Y} |0\rangle_A\right) \\ & + \sum_{Z_2} c_{\downarrow_y, Z_2} (R|\downarrow_y\rangle) \otimes |Z_2\rangle \otimes \left(X e^{-i(\pi/4 + \tilde{d}t)Y} |0\rangle_A\right). \end{aligned} \quad (\text{S14})$$

Fourth, the ancilla qubit is measured, and only the outcomes corresponding to $|0\rangle_a$ are retained. The resulting post-selected state becomes:

$$\begin{aligned} & \sum_{Z_2} c_{\uparrow_y, Z_2} (R|\uparrow_y\rangle) \otimes |Z_2\rangle \otimes \frac{\cos \tilde{d}t - \sin \tilde{d}t}{\sqrt{2}} |0\rangle_A \\ & + \sum_{Z_2} c_{\downarrow_y, Z_2} (R|\downarrow_y\rangle) \otimes |Z_2\rangle \otimes \frac{\cos \tilde{d}t + \sin \tilde{d}t}{\sqrt{2}} |0\rangle_A. \end{aligned} \quad (\text{S15})$$

Fifth, the inverse rotation R^{-1} is applied to the first qubit, and the ancilla qubit is discarded. This operation effectively implements the action of $\left[\left(\cos \tilde{d}t / \sqrt{2}\right) - \left(\sin \tilde{d}t / \sqrt{2}\right) P_{j,\uparrow_y} + \left(\sin \tilde{d}t / \sqrt{2}\right) P_{j,\downarrow_y}\right]$ on the left of the state $\sum_{Y_1, Z_2} c_{Y_1, Z_2} |Y_1\rangle \otimes |Z_2\rangle$. The same procedure is subsequently applied to the second qubit ($N = 2$). Upon measurement of the ancilla qubit in the $|0\rangle_a$ state for both sites, the final system state becomes:

$$\left(\frac{\cos \tilde{d}t}{\sqrt{2}}\right)^2 \exp(-idt H(\mathbf{h}, \boldsymbol{\delta})) |G\rangle_E \quad (\text{S16})$$

where the two-site Hamiltonian is $H(\mathbf{h}, \boldsymbol{\delta}) = -JZ_1 Z_2 - (h_x + \delta_x)(X_1 + X_2) - i(h_y + \delta_y)(Y_1 + Y_2)$ and the implemented operation results in a deterministic overall amplitude factor $\left(\cos \tilde{d}t / \sqrt{2}\right)^2$. To compensate for this fac-

tor and recover the target non-Hermitian dynamical evolution, the corresponding factor $\left(\cos \tilde{d}t/\sqrt{2}\right)^{-2}$ is calculated and applied to the measured data in the subsequent analysis.

To evaluate the $C[\rho(t)]$ in the two-site non-Hermitian Ising Hamiltonian (Eq. (1)), both the overlap $|\langle\varphi_0(dt)|\varphi_\delta(dt)\rangle|$ and the normalization factor $\langle\psi(t)|\psi(t)\rangle$ must be determined. The analysis proceeds in two steps. First, the normalization factor is given by

$$\begin{aligned} & \langle\psi(dt)|\psi(dt)\rangle \\ &= \frac{1}{2} (\langle\varphi_\delta(dt)|\varphi_\delta(dt)\rangle + \langle\varphi_0(dt)|\varphi_0(dt)\rangle) \\ &= \frac{1}{2} \left(\text{E}\langle G|e^{idtH^\dagger(\mathbf{h},\delta)}e^{-idtH(\mathbf{h},\delta)}|G\rangle_{\text{E}} + 1 \right) \\ &= \frac{1}{2} \left(\frac{\cos \tilde{d}t}{\sqrt{2}} \right)^{-4} \left(\sum_{j=0}^3 |c_j|^2 \right) + \frac{1}{2}, \end{aligned} \quad (\text{S17})$$

where the evolved state $e^{-idtH(\mathbf{h},\delta)}|G\rangle_{\text{E}} \equiv c_0|00\rangle + c_1|01\rangle + c_2|10\rangle + c_3|11\rangle$ is obtained by implementing both the unitary and non-unitary parts of the evolution operator $e^{-idtH(\mathbf{h},\delta)}$ within a quantum circuit. The factor $\left(\cos \tilde{d}t/\sqrt{2}\right)^{-4}$ derived from the non-unitary evolution contribution, is multiplied by the measured data according to the analytical formula to obtain the normalization factor.

Second, the overlap $|\langle\varphi_0(dt)|\varphi_\delta(dt)\rangle|$ is simplified as:

$$\begin{aligned} & |\langle\varphi_0(dt)|\varphi_\delta(dt)\rangle| \\ &= \left| \text{E}\langle G|e^{idtH^\dagger(\mathbf{h},0)}e^{-idtH(\mathbf{h},\delta)}|G\rangle_{\text{E}} \right| \\ &= \left| \text{E}\langle G|e^{-idtH(\mathbf{h},\delta)}|G\rangle_{\text{E}} \right| \\ &= \left| \langle 00|U_G^{-1}e^{-idtH(\mathbf{h},\delta)}U_G|00\rangle \right| \\ &= \left[\frac{\cos((h_y + \delta_y)dt)}{\sqrt{2}} \right]^{-2} |c'_0|, \end{aligned} \quad (\text{S18})$$

where c'_0 is the amplitude of the $|00\rangle$ component in the transformed state $U_G^{-1}e^{-idtH(\mathbf{h},\delta)}U_G|00\rangle$. In this representation, U_G prepares the ground state from $|00\rangle$, and its inverse projects the evolved state back onto $|00\rangle$, allowing direct extraction of the $C[\rho(t)]$. The final overlap value is obtained by multiplying the measured amplitude by the known factor $\left(\cos \tilde{d}t/\sqrt{2}\right)^{-2}$.

C. Adaptive-step trotterization scheme

In practice, imperfections in current quantum hardware introduce a trade-off: smaller time steps improve accuracy but necessitate deeper circuits, thereby amplifying noise. In this subsection, we adopt an adaptive-step trotterization scheme [37, 38] to balance these competing effects; it dynamically adjusts the step size dt to ensure the expectation value of the target observable remains within a predefined bound.

To employ adaptive-step trotterization scheme, we examine a two-site system ($N = 2$) and determine the maximum allowable variable step size dt . Specifically, we simulate the time evolution using IBM Qiskit [34], adjusting dt so that the deviation between the Trotterized and exact (non-Trotterized) evolutions remains below a tolerance of 10^{-2} . As shown in Fig. 3(b), the quantum circuit data of $C[\rho(t)]$ obtained under this condition demonstrate that the adaptive-step protocol effectively maintains accuracy while minimizing circuit depth.